JOURNAL OF GUIDANCE, CONTROL, AND DYNAMICS
Vol. 32, No. 6, November–December 2009

# Multiple-Model Adaptive Fault-Tolerant Control of a Planetary Lander

Jovan D. Bošković,[*] Joseph A. Jackson,[†] and Raman K. Mehra[‡]
*Scientific Systems Company, Inc., Woburn, Massachusetts 01801*
and
Nhan T. Nguyen[§]
*NASA Ames Research Center, Moffet Field, California 94035*

DOI: 10.2514/1.42719

**In this paper we present an approach to fault-tolerant control based on multiple models, switching, and tuning and its implementation to a hardware-in-the-loop simulation of Delta Clipper Experimental dynamics. The Delta Clipper Experimental is characterized by large control input redundancy, which made it an ideal test bed for evaluation of advanced fault-tolerant and adaptive reconfigurable control strategies. The overall failure detection, identification, and accommodation architecture is an upgraded version of our Fast Online Actuator Reconfiguration Enhancement (FLARE) system. The FLARE approach is based on representing different possible fault and failure scenarios using multiple observers, such that the case of nominal (no-failure) operation is covered along with the loss-of-effectiveness, lock-in-place, and hardover failures of the flight control effectors. Based on a suitably chosen performance criterion, the FLARE system quickly detects single or multiple failures and reconfigures the controls, thus achieving either the original desired performance or graceful performance degradation. In the first stage of the project, the FLARE system was tested on a medium-fidelity simulation of Delta Clipper Experimental dynamics, resulting in excellent performance over a large range of single and multiple faults and failures. Following that, in collaboration with Boeing Phantom Works, the FLARE run-time code was installed at their site and tested on a hardware-in-the-loop test bed consisting of an electromechanical actuator actuating a gimballed engine as a part of a simulation of the Delta Clipper Experimental dynamics. A large number of hardware-in-the-loop simulations were run to cover a dense test-case matrix, including cases of up to 10 simultaneous control effector failures. In all cases FLARE was able to quickly and accurately detect the failures and reconfigure the controls, resulting in excellent overall system performance. In this paper we describe the Delta Clipper Experimental and its dynamics model, along with the multiple models, switching, and tuning based modification of our FLARE system. This is followed by a description of the experimental test bed and a discussion of the results obtained through hardware-in-the-loop testing.**

## Nomenclature

$a$ = lateral distance from engines to c.g., m
$b$ = longitudinal distance from engines to c.g., m
$c$ = lateral distance from thrusters to c.g., m
$c_1$, $c_2$ = performance index gains
$d$ = longitudinal distance from thrusters to c.g., m
$F_{ab}$ = force along $a$ axis due to actuator $b$, N
$G_o$ = nonlinear control derivative matrix
$g$ = acceleration due to gravity, $9.81\ \mathrm{kg \cdot m/s^2}$
$I_j(t)$ = performance index of estimator $j$ at time $t$
$J$, $J_{ii}$ = inertial matrix, elements with $J_{xx}$, $J_{yy}$, and $J_{zz}$ on the diagonal, $\mathrm{kg/m^2}$
$K$, $k_i$ = loss-of-effectiveness failure diagonal matrix, $i$th value
$m$ = mass, kg
$P_i$ = magnitude of $i$th reaction control system thruster, N
$r_{ab}$ = component along $a$ axis of the $b$th reaction control system thruster, m
$r_{(\cdot)}$ = commands for the reference trajectory, m/s
$T_i$ = thrust magnitude from engine $i$, N
$t_{Fi}$ = time of failure injection on actuator $i$, s
$\mathbf{u}$ = control inputs, $u_1$–$u_4$: engine thrust, N; $u_5$–$u_{12}$: gimbal angles, rad; $u_{13}$–$u_{16}$: thrust from reaction control system, N
$\mathbf{u}_c$ = commanded control input vector
$\mathbf{x}$ = system state
$x$, $y$, $z$ = position coordinates in the inertial frame, m
$\alpha_{Ri}$ = radial angle of $i$th engine gimbal, rad
$\alpha_{Ti}$ = tangential angle of $i$th engine gimbal, rad
$\gamma$ = estimator adaptation gain
$\Delta$, $\delta$ = normalization matrix, factor
$\Theta$, $\theta_i$ = lumped failure parameter diagonal matrix, $i$th value
$\Lambda$, $\lambda_i$ = actuator gain diagonal matrix, $i$th value, 1/s
$\Sigma$, $\sigma_i$ = lock-in-place failure diagonal matrix, $i$th value
$\tau_{ab}$ = torque about $a$ axis due to actuator $b$, Nm
$\boldsymbol{\omega}$ = attitude vector, $[\phi, \theta, \psi]^T$, rad

## I. Introduction

IN THE recent past there has been much interest in the design and implementation of failure detection, identification, and reconfiguration (FDIR) techniques to aerospace vehicles under subsystem and component failures and damages [1–5]. Although many of the proposed techniques have been demonstrated as effective control reconfiguration strategies for accommodation of different types of failures and damages in aerial vehicles, space vehicles such as planetary landers have attracted comparably less attention in the existing literature.

---

Presented as Paper 7290 at the AIAA Guidance, Navigation and Control Conference and Exhibit, Honolulu, HI, 18–21 August 2008; received 23 January 2009; revision received 18 August 2009; accepted for publication 20 August 2009.

[*] Intelligent & Autonomous Control Systems Group Leader, 500 West Cummings Park, Suite 3000; jovan@ssci.com. Senior Member AIAA.

[†] Research Engineer, Intelligent & Autonomous Controls Systems, 500 West Cummings Park, Suite 3000; jjackson@ssci.com. Member AIAA.

[‡] President and CEO, 500 West Cummings Park, Suite 3000; rkm@ssci.com. Member AIAA.

[§] Principal Research Scientist, Mail Stop 269-4; Nhan.T.Nguyen@nasa.gov. Associate Fellow AIAA.

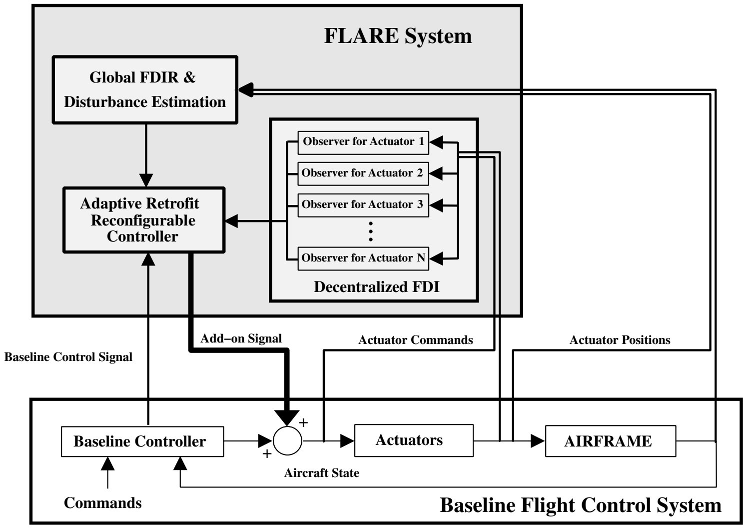

**Fig. 1 Structure of the FLARE system.**

The onboard FDIR problem is particularly important for space exploration vehicles that require minimal downtime for repairs during a mission. Our focus has been on the Delta Clipper Experimental (DC-X) [6–10], which was designed by McDonnell Douglas in the early 1990s as a one-third-scale prototype for a proposed vertical takeoff and landing (VTOL) reusable launch vehicle capable of single stage to orbit.[¶]

This work presents hardware-in-the-loop (HWIL) simulation results using an adaptive reconfigurable flight control design for a DC-X control design model consisting of translational and attitude dynamics, four gimballed engines, four reaction control system (RCS) thrusters for attitude control, and actuator dynamics with position and rate limits. A variety of failures were injected into the model, and our modified FDIR system [11,12], introduced in the following paragraph and continued in Sec. IV, was implemented and tested in hardware-in-the-loop simulations to evaluate the overall system performance [13]. Special consideration was given to determining the total number of failures that could be accommodated using the available actuator redundancy.

We have recently modified our baseline Fast Online Actuator Reconfiguration Enhancement (FLARE) system to include a new failure parametrization [14], as well as a multiple-model failure detection and identification (FDI) based upon previous work [15]. Central to FLARE, shown in Fig. 1, are FDI observers based on the new failure parametrization that describes a large class of failures in terms of a single uncertain parameter. The FLARE system achieves very fast detection and identification of failures in flight control actuators and effective control reconfiguration in the presence of single or multiple actuator failures and control effector damages even while rejecting external disturbances. The FLARE system combines different FDIR algorithms with a disturbance rejection mechanism within a retrofit control architecture. In collaboration with Boeing Phantom Works, the performance of the previous version of the FLARE system was extensively evaluated using high-fidelity and piloted simulators [11]. The FLARE system achieved excellent response in the presence of severe flight-critical control effector failures and received excellent handling quality ratings from the pilot. The FLARE system was used as a basis for FDIR design in the context of the DC-X model.

The sections that follow describe the plant and actuator dynamic model, trajectory design, failure injection, reconfigurable control design, and simulation results.

## II. Delta Clipper Experimental Model Representation

The DC-X, shown during an early flight test in Fig. 2, is actuated by four liquid-propelled engines, which are affixed to electromechanical actuators (EMAs) driving two gimbal angles for each engine, and four RCS thrusters. The basic schematic of the vehicle is shown in Fig. 3.

For each engine, three control inputs are available: thrust magnitude ($T$), radial gimbal angle ($\alpha_R$), and tangential gimbal angle ($\alpha_T$). The radial gimbal angle is measured positive outward from the craft, whereas the tangential gimbal angle is measured positive counterclockwise when looking from the nose toward the base of the vehicle. The four engines are numbered, beginning with engine 1 along the $x$ axis and engines 2–4 proceeding counterclockwise around the perimeter of the vehicle. The subscripts $e_1 \cdots e_4$ denote the engines, whereas $t_1 \cdots t_4$ denote RCS thrusters.

Next we describe a model of DC-X dynamics based upon its detailed simulation provided by the Boeing Phantom Works team.

Based upon angular definitions in Fig. 3, the forces acting on the body can be calculated as follows:

**Fig. 2 Delta Clipper Experimental at takeoff (courtesy of NASA).**

---

[¶]Data on the McDonnell Douglas DC-X is available online at http://en.wikipedia.org/wiki/McDonnell_Douglas_DC-X [retrieved 4 Sept. 2009].

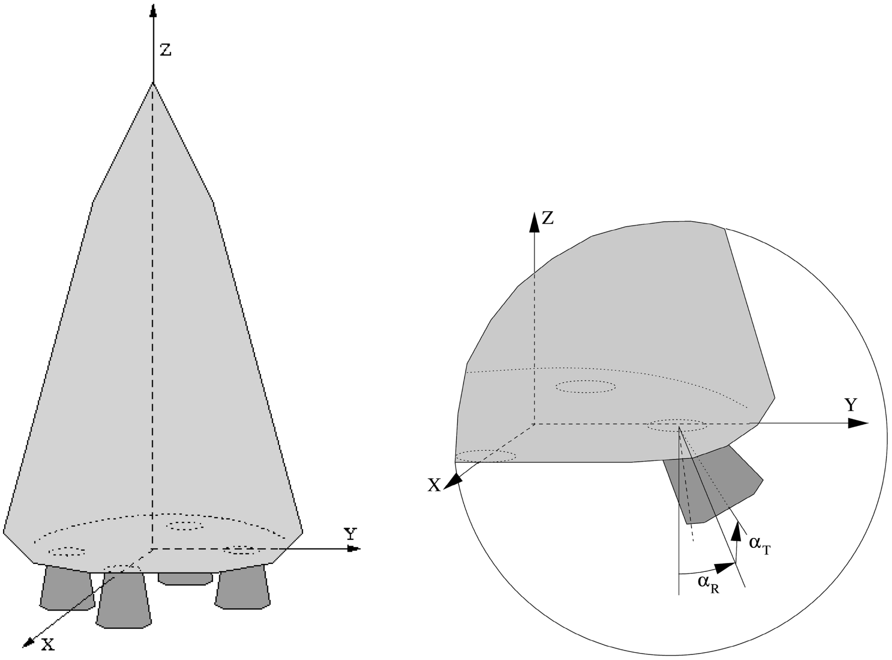

**a) Coordinate axis alignment** **b) Positive engine vectoring conventions**

**Fig. 3 Schematic of DC-X. a) The engines were modeled to be coincident along the *x* and *y* axes. As a VTOL vehicle, thrust vectoring intends to maintain vertical orientation during ascent and descent. b) The thrust delivered from each engine can be vectored using a two-axis gimbal mechanism to direct the thrust radially by adjusting $\alpha_R$ or tangentially by adjusting $\alpha_T$.**

$$\begin{gathered}
F_{xe1} = -T_1 \sin\alpha_{R1}, \qquad F_{ye1} = -T_1 \cos\alpha_{R1} \sin\alpha_{T1} \\
F_{xe2} = T_2 \cos\alpha_{R2} \sin\alpha_{T2}, \qquad F_{ye2} = -T_2 \sin\alpha_{R2} \\
F_{xe3} = T_3 \sin\alpha_{R3}, \qquad F_{ye3} = -T_3 \cos\alpha_{R3} \sin\alpha_{T3} \\
F_{xe4} = -T_4 \cos\alpha_{R4} \sin\alpha_{T4}, \qquad F_{ye4} = T_4 \sin\alpha_{R4} \\
F_{zei} = T_i \cos\alpha_{Ri} \cos\alpha_{Ti}, \quad \text{for } i = 1, 2, 3, 4
\end{gathered} \tag{1}$$

where $F_{xe1}$ defines the force generated in the $x$ direction by engine 1, and so on. The RCS thrusters are installed so that all resultant forces are applied in the $x$–$y$ plane of the body frame. Hence, the thrusters are used for attitude control. The resultant thrust vectors from the RCS are designed primarily to give a greater amount of torque to the pitch and roll of the vehicle. The thrusters also produce minimal yaw moment on the vehicle, because the resultant vector from each thruster is not incident upon the vehicle's center of gravity.

The contributions of each thruster to the total force acting on the vehicle is calculated as follows:

$$F_{xti} = r_{xi} P_i, \qquad F_{yti} = r_{yi} P_i, \qquad i = 1, 2, 3, 4$$

where $r_{xi}$ and $r_{yi}$ are the components of RCS along the body frame $x$ and $y$ axes, respectively, and $P_i$ are the thrust magnitudes from each RCS thruster.

For the representation of the plant, the forces are grouped according to the coordinate axis along which they are applied to yield the net force in each direction in body coordinates. Assuming a vertical world-frame orientation, the component force due to gravity is in the negative $z$ direction. The elements of the force vector, $\mathbf{F} = [F_x \quad F_y \quad F_z]^\top$, are expressed as sums of forces from the engines and RCS thrusters:

$$\begin{gathered}
F_x = \sum_{i=1}^{4} (F_{xei} + F_{xti}), \quad F_y = \sum_{i=1}^{4} (F_{yei} + F_{yti}) \\
F_z = \sum_{i=1}^{4} (F_{zei} + F_{zti}) - mg
\end{gathered} \tag{2}$$

Torque is defined by $\tau_i = r_i \times F_i$, with $\tau_i = [\tau_{xi} \quad \tau_{yi} \quad \tau_{zi}]^\top$. Given the lateral and longitudinal distances, $a$ and $b$, respectively, from the center of gravity to the point at which the engine thrust exerts forces on the vehicle, the cross products representing the torques from the four engines about the principal axes result in

$$\begin{aligned}
\tau_{xe} &= bF_{ye1} + bF_{ye2} + aF_{ze2} + bF_{ye3} + bF_{ye4} - aF_{ze4} \\
\tau_{ye} &= -bF_{xe1} - aF_{ze1} - bF_{xe2} - bF_{xe3} + aF_{ze3} - bF_{xe4} \\
\tau_{ze} &= aF_{ye1} - aF_{xe1} - aF_{ye3} + aF_{xe4}
\end{aligned} \tag{3a}$$

Let $c$ denote the lateral distance from the thrusters to the center of gravity, as in Fig. 4, and let $d$ denote the longitudinal (out-of-plane) distance from the thrusters to the center of gravity. The sum of the torques from the four thrusters can be computed as

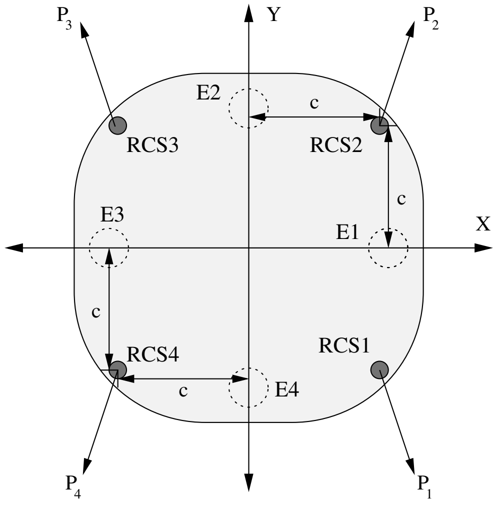

**Fig. 4 The RCS thrusters are oriented to provide adjustments to the vehicle's roll and pitch. Each thruster is characterized by a distance *c* along the *x* and *y* axes from the *z* axis (*z* axis assumed coincident with the center of gravity) and a distance *d* along the *z* axis from the center of gravity. The angles of actuation from the RCS relative to the DC-X are fixed, but the magnitude of the RCS thrust can be changed through commanding. Here E1–E4 denote the locations of the engines, whereas RCS1–RCS4 denote the locations of the RCS thrusters.**

$$\begin{aligned}\tau_{xt} &= -dF_{yt1} - dF_{yt2} - dF_{yt3} - dF_{yt4}\\ \tau_{yt} &= dF_{xt1} + dF_{xt2} + dF_{xt3} + dF_{xt4}\\ \tau_{zt} &= -cF_{xt1} + cF_{yt1} - cF_{xt2} + cF_{yt2} - cF_{xt3}\\ &\quad + cF_{yt3} - cF_{xt4} + cF_{yt4}\end{aligned} \tag{3b}$$

The overall torque about each body-frame axis is simply the sum of the torque from the engines in Eq. (3a) and the torque from the thrusters in Eq. (3b).

Let the attitude dynamics be of the form $J\dot{\omega} = \sum \tau$, where, due to small-angle approximation, we assume that $\boldsymbol{\omega} = [\phi \quad \theta \quad \psi]^\top$ and that the Coriolis term $\omega^\times J\omega$ can be neglected. The system's position and attitude dynamics are now of the following form:

$$\begin{aligned}\ddot{x} &= (1/m)F_x, \qquad \ddot{y} = (1/m)F_y, \qquad \ddot{z} = (1/m)F_z\\ \dot{\phi} &= (1/J_{xx})\tau_x, \qquad \dot{\theta} = (1/J_{yy})\tau_y, \qquad \dot{\psi} = (1/J_{zz})\tau_z\end{aligned} \tag{4}$$

## III. Actuator Dynamics Under Failures

The actuator dynamics are assumed to be approximately first order and are modeled by means of a single gain $\lambda_{ai} > 0$. The gains for the engines are an order of magnitude smaller than those of the electromechanical actuators.

Three basic actuator fault modes are included in the simulation: 1) lock in place (LIP) ($u(t)$ is locked at its current position), 2) hardover ($u(t)$ locks at the position limit), and 3) loss of effectiveness (LOE) (actuator gain decreases from $k = 1$ to a value of $k \in (0, 1)$).

To simulate engine or gimbal failures, an appropriate failure model is used. First, a LIP matrix $\Sigma$ is defined as $\Sigma = \mathrm{diag}([\sigma_1 \quad \sigma_2 \quad \cdots \quad \sigma_m])$, where $\sigma_i(t) = 1$ for $t < t_{Fi}$ and $\sigma_i(t) = 0$ for $t \geq t_{Fi}$. This matrix is initialized to an $n \times n$ identity matrix, where $n$ is the number of control inputs. When a LIP failure occurs at the $j$th input, the value at $\Sigma(j, j)$ is set to zero. For convenience, the value at $\Sigma(j, j)$ will also be referred to as $\sigma_j$. To include LOE within the model, an input effectiveness matrix $K$ is chosen as a diagonal matrix for which the elements describe the effectiveness of each control input. $K$ is also initialized as an $n \times n$ identity matrix.

Now the actuator dynamics including the failure model is of the form

$$\dot{\mathbf{u}} = -\Lambda_a[(\mathbf{u} - K\Sigma\mathbf{u}_c) + (I - \Sigma)\mathbf{u}] \tag{5}$$

where $\mathbf{u}_c$ is the controller output, $\mathbf{u}$ is the output of the actuator, $\Lambda_a = \mathrm{diag}[\lambda_{a1} \quad \lambda_{a2} \quad \cdots \quad \lambda_{am}]$ is the matrix of actuator gains, and $K = \mathrm{diag}([k_1 \quad k_2 \quad \cdots \quad k_m])$, where $k_i \in [\epsilon_i, 1]$ and $\epsilon_i \ll 1$.

## IV. Failure Detection and Identification

The algorithms for estimating the unknown failure-related parameters associated with DC-X actuators are based on the basic FLARE design augmented with the new failure parametrization-based FDI observers and are described below.

### A. Estimation of Failure-Related Parameters

#### 1. *Observer*

The observers for the model [Eq. (5)] are based on the new failure parametrization [14] of the form

$$\dot{\mathbf{u}} = -\Lambda_a\mathbf{u} + \Lambda_a(\Theta\mathbf{u}_c + \Delta\mathbf{u}) \tag{6}$$

where $\Theta = \mathrm{diag}[\theta_1 \quad \theta_2 \quad \cdots \quad \theta_m]$,

$$\Delta = \mathrm{diag}\left(\tfrac{\delta}{\theta_1+\delta} \quad \tfrac{\delta}{\theta_2+\delta} \quad \cdots \quad \tfrac{\delta}{\theta_m+\delta}\right) \tag{7}$$

and $0 < \delta \ll 1$. It is seen that, when $\theta_i = 0$, $\dot{u}_i = 0$. When $\theta_i = \bar{\theta}_i > 0$, we have $\dot{u}_i \cong -\lambda_{ai}(u_i - \bar{\theta}_i u_{ci})$, because $\delta\bar{u}_i/(\bar{\theta}_i + \delta) \cong 0$. Hence, this model has the desired properties of covering both the LIP and LOE cases for a sufficiently small $\delta$.

Now the observer is chosen in the following form:

$$\dot{\hat{\mathbf{u}}} = -\Lambda_a\mathbf{u} + \Lambda_a(\hat{\Theta}\mathbf{u}_c + \hat{\Delta}\mathbf{u}) - \Lambda_o\tilde{\mathbf{u}} \tag{8}$$

where $\tilde{\mathbf{u}} = \hat{\mathbf{u}} - \mathbf{u}$, $\hat{\Theta} = \mathrm{diag}[\hat{\theta}_1 \quad \hat{\theta}_2 \quad \cdots \quad \hat{\theta}_m]$,

$$\hat{\Delta} = \mathrm{diag}\left(\tfrac{\delta}{\hat{\theta}_1+\delta} \quad \tfrac{\delta}{\hat{\theta}_2+\delta} \quad \cdots \quad \tfrac{\delta}{\hat{\theta}_m+\delta}\right) \tag{9}$$

and $\Lambda_o = \mathrm{diag}[\lambda_{o1} \quad \lambda_{o2} \quad \cdots \quad \lambda_{om}]$, where $\lambda_{oi} > 0$.

#### 2. *Adaptive Laws*

Adaptive laws are of the following form:

$$\dot{\hat{\theta}}_i = \mathrm{Proj}_{[0,1]}\{-\gamma_i\omega_i\tilde{u}_i\}, \qquad \hat{\theta}_i(0) = 1 \tag{10}$$

where Proj$\{\cdot\}$ denotes the projection operator, which keeps the estimates of $\hat{\Theta}(t)$ inside the interval [0, 1] for all time; $\gamma_i > 0$ denote adaptive gains; and

$$\omega_i = u_{ci} - \frac{\delta u_i}{(\hat{\theta}_i + \delta)^2}$$

As shown recently [14], these adaptive laws result in a stable estimator.

### B. Multiple-Model-Based Failure Detection and Identification

As with many design problems, scaling plays a major role in the computations of the estimators and adaptation laws. To improve the performance of the controller, scaling the terms such that the thrust and angular measurements have a similar order of magnitude is desirable. Nominal thrusts are of the order of 50,000 N, whereas the angles' limits are approximately 0.14 rad.

An additional issue here is that, due to the size of the thrust signals, the effect of loss of effectiveness is very different than that of the lock-in-place failures. It was found that a single FDI observer with a single adjustable parameter (recall the $\theta$ parametrization described earlier) is not well suited to cover all the cases of loss of effectiveness and lock in place. We hence tested a new approach to FDI based on a multiple models, switching, and tuning (MMST) technique pioneered by Narendra and Balakrishnan [16].

The concept of MMST is based on the idea of describing the dynamics of the system using different models for different operating regimes; such models identify the current dynamics of the system and are consequently referred to as the identification models. The basic idea is to set up such identification models and corresponding controllers in parallel, Fig. 5, and to devise a suitable strategy for switching among the controllers to achieve the desired control

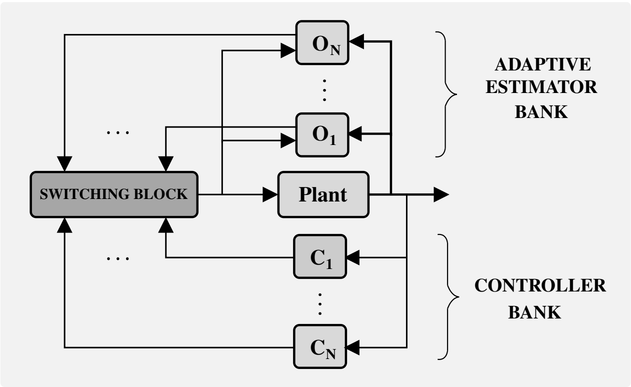

**Fig. 5 Structure of the multiple-model-based controller: outputs of the parallel observers $O_1, O_2, \ldots, O_N$ are used to find the observer that is closest, in some sense, to the corresponding controller from $C_1, C_2, \ldots, C_N$.**

objective. While the plant is being controlled using one of these controllers, the identification models are run in parallel to generate some measure of the corresponding identification errors and find a model which is, in some sense, closest to the current operating regime of the plant. Once such a model is found, the switching mechanism switches to (or stays at) the corresponding controller, for which the switching interval is a parameter chosen by the designer.

The main feature of this approach is that, in linear time-invariant systems, if the switching interval is chosen to be strictly greater than zero, it results in a stable overall system in which asymptotic convergence of the output error to zero is guaranteed under relatively mild conditions [16]. In addition, if adaptive control is used and the controller parameters are adjusted using adaptive algorithms with projection, the overall system is robust to different perturbations, including bounded external disturbances, time variations of plant parameters, and some classes of unmodeled dynamics. As also shown through extensive simulations, the performance of the overall switching system can be dramatically improved as compared with that achieved using a single adaptive controller. Several different structures of the overall switching system are possible. One includes all fixed parallel models and controllers and results in the boundedness of the output error provided at least one of the models is sufficiently close to the model describing the current dynamics of the plant. Such fixed models and controllers can also be combined with an adaptive controller in the sense that the system first switches to the fixed model closest to the plant and then adapts from there. This results in substantially improved overall performance and in a stable overall system in which asymptotic convergence of the output error to zero is guaranteed. Another possibility is to employ all adaptive models, which yields the same stability result, but is more computationally intensive.

In all these cases, the switching algorithm is implemented by first calculating the following performance indices:

$$\begin{aligned} I_j(t) &= c_1\|\hat{\mathbf{e}}_j(t)\|^2 \\ &\quad + c_2\int_{t_o}^{t}\exp(-\lambda(\tau - t_o))\,\|\,\hat{\mathbf{e}}_j(\tau)\|^2\,\mathrm{d}\tau, \qquad j = 1, 2, \ldots, N \end{aligned} \tag{11}$$

where observer state errors are denoted for the $j$th observer by$\hat{\mathbf{e}}_j = \hat{\mathbf{x}}_j - \mathbf{x}$, $c_1 > 0$, $c_2 > 0$, and $\lambda > 0$.

The scheme is now implemented by calculating and comparing these indices every $t_s$ instants, finding the minimum, and switching to the corresponding controller. In the case of fixed models and controllers, the overall scheme is guaranteed to result in bounded errors as long as $T_{\min} \geq \tau_s \geq \delta > 0$, where $T_{\min}$ is some minimum-length time interval needed to guarantee error boundedness.

In the context of reconfigurable control design in the presence of parametric uncertainties and/or sensor, actuator, and structural failures, the identification models (observers) $O_1, \ldots, O_N$ from Fig. 5 correspond to different regions in the parameter space, characterizing different types of failures, whereas $C_1, \ldots, C_N$ denote the corresponding controllers.

In the context of FDI design for the DC-X model, we used the MMST approach with a model that corresponds to the nominal (no-failure) case and models for LIP and LOE failures. The best estimate at every instant, as selected by the MMST subsystem, is used in the control law. A summary of the equations for each estimator is found in Table 1.

The best estimator is chosen according to the performance indices from Eq. (11), calculated using the errors from each estimator. The observer with the best (minimum) performance index is used in the control law. The failure parameter estimate is assigned according to

$$\hat{\theta}_i(t) = \begin{cases} 1, & \text{if } I_{1i}(t) \text{ is min} \\ k_i(t) & \text{if } I_{2i}(t) \text{ is min} \\ \sigma_i(t) & \text{if } I_{3i}(t) \text{ is min} \end{cases} \tag{12}$$

## V. Control Design

The reconfigurable control design starts with the design of a baseline controller. The latter is used as a basis for the adaptive controller that at every instant uses estimates generated by FDI observers. We describe the baseline control design next.

### A. Baseline Controller

In the no-failure case, the nonlinear state-space model of the DC-X dynamics can be represented in a compact form as

$$\dot{\boldsymbol{x}}_1 = \boldsymbol{x}_2 \tag{13}$$

$$\dot{\boldsymbol{x}}_2 = G_o(u) + [0 \quad 0 \quad -g \quad 0 \quad 0 \quad 0]^\top \tag{14}$$

where $\boldsymbol{x}_1$ denotes the states corresponding to the 6 deg of freedom in both translation and rotation, $\boldsymbol{x}_2$ denotes the corresponding rates, and $u \in \mathbb{R}$ for the 16 actuators. It is seen that this system can be rewritten as

$$\ddot{\boldsymbol{x}}_1 = G_o(u) + \bar{g} \tag{15}$$

where $\bar{g} = [0 \quad 0 \quad -g \quad 0 \quad 0 \quad 0]^\top$.

### B. Reference Model Design

A typical test maneuver for DC-X follows a basic climb, $x$ and $y$ translation, and then a descent path. The desired closed-loop dynamics along the $z$ axis are of the form

$$\ddot{z}^* = -k_2\dot{z}^* - k_1 z^* + k_1 r_z \tag{16}$$

where $z^*$, $\dot{z}^*$, and $\ddot{z}^*$ represent the desired position, velocity, and acceleration, $r_z$ is the command in the $z$ direction, and $k_i > 0$. Each of the relationships in Eq. (4) has an associated equation of the form in Eq. (16). The resulting reference model is of the form

$$\dot{x}^*_{1i} = x^*_{2i} \tag{17}$$

$$\dot{x}^*_{2i} = -k_1 x^*_{1i} - k_2 x^*_{2i} + k_1 r_i, \qquad i = 1, 2, \ldots, 6 \tag{18}$$

In the no-failure case, the actuator dynamics are of the form

$$\dot{\mathbf{u}} = -\Lambda_a(\mathbf{u} - \mathbf{u}_c)$$

where $\Lambda_a = \mathrm{diag}[\lambda_{a1} \quad \lambda_{a2} \quad \cdots \quad \lambda_{am}]$ and $\lambda_{ai} > 0$.

Because $G_o$ cannot be inverted analytically, using a previously reported approach [17], we take another derivative of the above equation to obtain:

$$\dddot{\boldsymbol{x}}_1 = G(\mathbf{u})\dot{\mathbf{u}} \tag{19}$$

where $G = \frac{\partial G_o(\mathbf{u})}{\partial \mathbf{u}}$.

Because the order of the system has increased, the reference model is also changed as

**Table 1 Multiple-model-based FDI observers**

| | Actuator failure dynamics | Observer dynamics |
|---|---|---|
| Nominal | $\dot{\mathbf{u}} = -\Lambda_a(\mathbf{u} - \mathbf{u}_c)$ | $\dot{\hat{\mathbf{u}}} = -\Lambda_a(\mathbf{u} - \mathbf{u}_c) - \lambda_{\mathrm{nom}}(\hat{u}_1 - \mathbf{u})$ |
| LOE | $\dot{\mathbf{u}} = -\Lambda_a(\mathbf{u} - K\mathbf{u}_c)$ | $\dot{\hat{\mathbf{u}}} = -\Lambda_a(\mathbf{u} - \mathrm{diag}(\hat{k})\mathbf{u}_c) - \lambda_{\mathrm{loe}}(\hat{\mathbf{u}} - \mathbf{u})$<br>$\dot{\hat{k}} = -\gamma_{\mathrm{loe}}\hat{e}_2\mathbf{u}_c$ |
| LIP | $\dot{\mathbf{u}} = -\Lambda_a\Sigma(\mathbf{u} - \mathbf{u}_c)$ | $\dot{\hat{\mathbf{u}}} = -\Lambda_a\mathrm{diag}(\hat{\sigma})(\mathbf{u} - \mathbf{u}_c) - \lambda_{\mathrm{lip}}(\hat{\mathbf{u}} - \mathbf{u})$<br>$\dot{\hat{\sigma}} = \gamma_{\mathrm{lip}}\hat{e}_3(\mathbf{u} - \mathbf{u}_c)$ |

$$\dot x^*_{1i} = x^*_{2i} \tag{20}$$

$$\dot x^*_{2i} = x^*_{3i} \tag{21}$$

$$\dot x^*_{3i} = -\bar k_{1i} x^*_{1i} - \bar k_{2i} x^*_{2i} - \bar k_{3i} x^*_{3i} + \bar k_{1i} r_i, \qquad i = 1, 2, \ldots, 6 \tag{22}$$

where $\bar k_{ij} > 0$ and $\bar k_{2j} \bar k_{3j} > \bar k_{1j}$. We also let

$$\eta^*_i = -\bar k_{1i} x_{1i} - \bar k_{2i} x_{2i} - \bar k_{3i} x_{3i} + \bar k_{1i} r_i, \qquad i = 1, 2, \ldots, 6 \tag{23}$$

and $\boldsymbol{\eta}^* = [\eta^*_1 \quad \eta^*_2 \quad \ldots \quad \eta^*_6]^T$.

Assuming that $G$ is invertible on a domain, we design the following dynamic controller:

$$\mathbf{u}_c = \mathbf{u} + (G(\mathbf{u})\Lambda_a)^\top (G(\mathbf{u})\Lambda_a (G(\mathbf{u})\Lambda_a)^\top)^{-1} \boldsymbol{\eta}^* \tag{24}$$

The resulting closed-loop system is simply

$$\ddot{\mathbf{x}}_1 = \boldsymbol{\eta}^* \tag{25}$$

More details regarding the dynamic controller technique in the adaptive control context can be found in our previous work [17].

It is interesting to note that, due to the first-order actuator dynamics, the actual control input $\mathbf{u}_c$ is static, that is, there is no need to generate it as a solution of a differential equation because it can be directly computed from Eq. (24). In addition, because $\Lambda$ is known, even when $\mathbf{u}$ is not measurable, we can build a simple observer to estimate $\mathbf{u}$:

$$\dot{\hat{\mathbf{u}}} = -\Lambda_a(\hat{\mathbf{u}} - \mathbf{u}_c)$$

so that, for zero initial conditions, $\hat u(t) = u(t)$ for all time.

### C. Ideal Reconfigurable Controller for the Case of Known Failures

An important step in adaptive reconfigurable control design is to design a fixed reconfigurable controller that assumes that the failure-related parameters are completely known. By studying the resulting closed-loop control system, important information about *reconfigurability* can be obtained, that is, the extent of failure(s) that can be accommodated using the ideal reconfigurable controller under control input constraints. If, for a specific failure, the control inputs saturate, there is a way of assuring graceful performance degradation by changing the reference model, or the command inputs, or both. Hence, preliminary analysis using the ideal reconfigurable controller is important because it results in conditions under which a solution to the reconfigurable control problem exists.

When the failure-related parameters are known, the plant dynamics are of the form

$$\ddot{\mathbf{x}} = G(\mathbf{u})\Lambda_a[\Sigma(K\mathbf{u}_c - \mathbf{u})] \tag{26}$$

and the reconfigurable controller is hence of the form

$$\mathbf{u}_c = (G(\mathbf{u})\Lambda_a \Sigma K)^\top (G(\mathbf{u})\Lambda_a \Sigma K (G(\mathbf{u})\Lambda_a \Sigma K)^\top)^{-1} \times (\boldsymbol{\eta}^* - G(u)\Lambda_a \Sigma \mathbf{u})$$

### D. Adaptive Reconfigurable Controller

Now the adaptive reconfigurable controller is chosen in the form

$$\mathbf{u}_c = (G(\mathbf{u})\Lambda_a \hat\Theta)^T (G(\mathbf{u})\Lambda_a \hat\Theta^2 G(\mathbf{u})^T)^{-1} \times \left( \boldsymbol{\eta}^* - \sum_{i=1}^{n} g_i(\mathbf{x}) \lambda_{ai} \frac{\delta u_i}{\hat\theta_i + \delta} \right)$$

As shown previously [14], this control law, in conjunction with these estimator and adaptive laws, assures closed-loop stability and asymptotic convergence of the tracking error to zero.

## VI. High-Fidelity Simulation Setup

The modified FLARE system described in the previous section was used to control the DC-X planetary lander under different types of actuator failures.

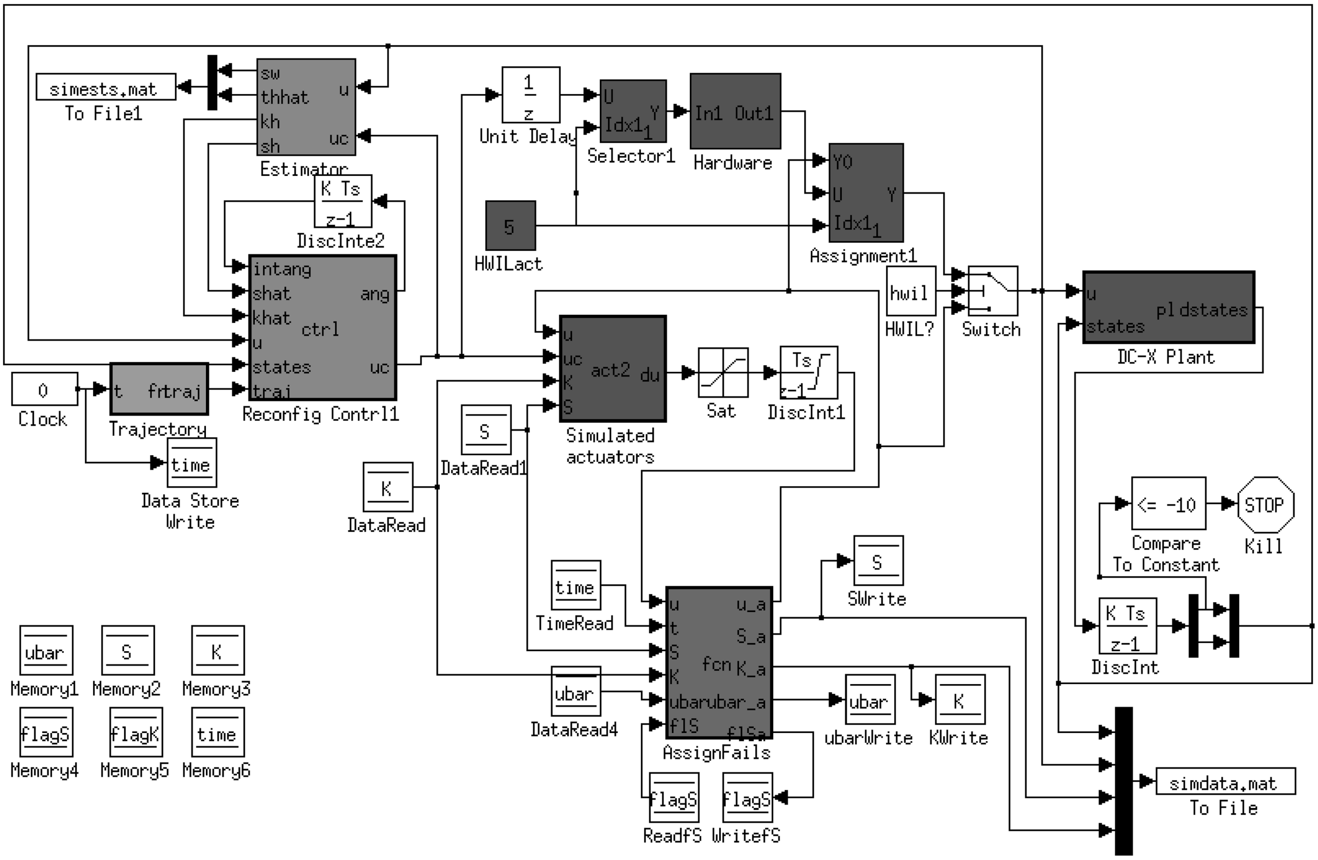

Fig. 6 Simulink model. The trajectory generator, controller/estimator, actuators, failure generation block, and DC-X are highlighted.

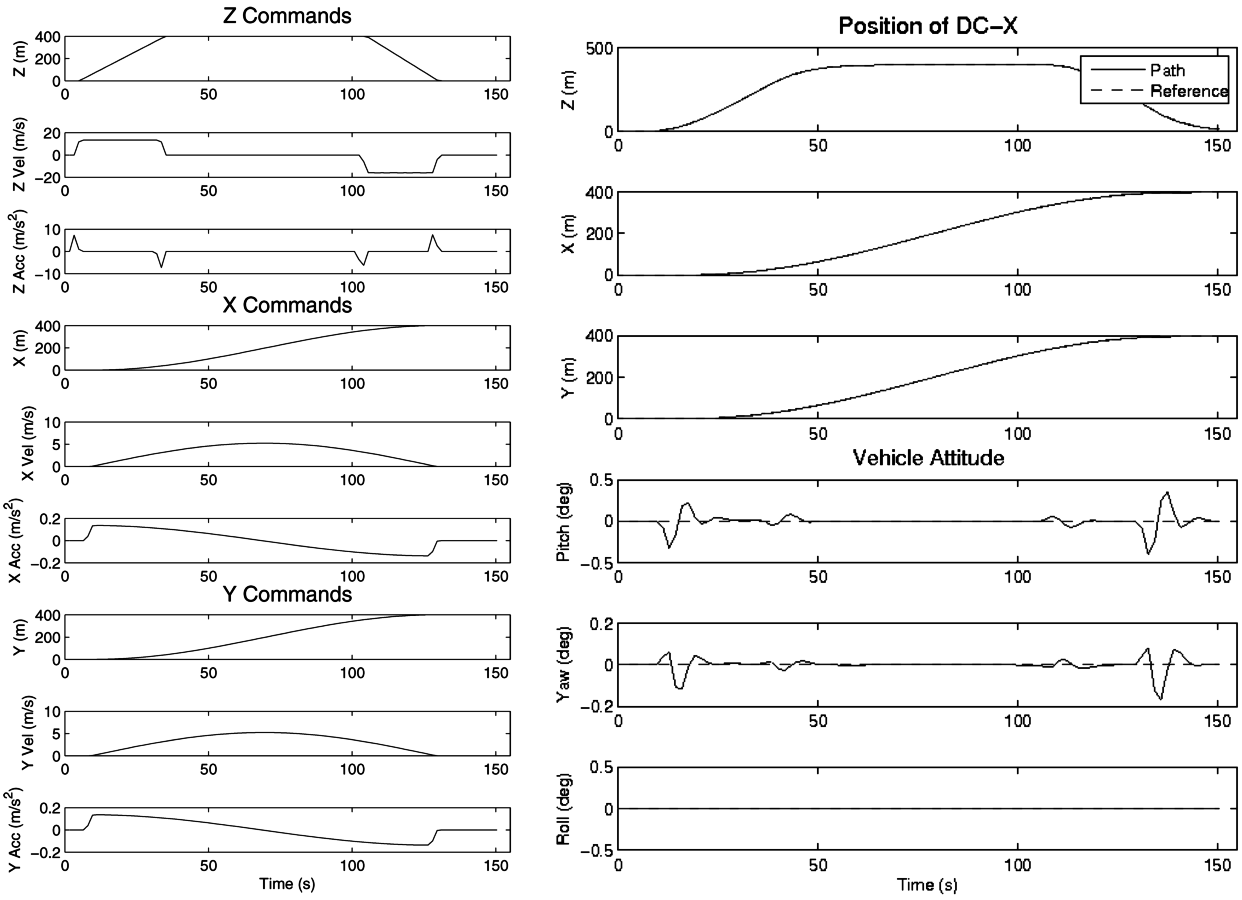

**a) Reference trajectories** **b) States using baseline controller**

**Fig. 7 Reference trajectories in $x$, $y$, and $z$, and the baseline 6 deg of freedom control response: a) trajectory design for position, velocity, and acceleration of $Z$, $X$, and $Y$ axes; and b) baseline output to trajectory using baseline controller and a healthy plant (note the dashed reference model output compared with the state output).**

The high-fidelity simulation of DC-X dynamics was obtained from Boeing Phantom Works. The simulation is based on a high-fidelity model that describes the relationship between the states of the vehicle and the main engine propulsive thrust, gimbal angles, and RCS thrusters and contains actuator dynamics and position and rate constraints.

Because of large differences in the magnitudes of the engine-generated thrust and gimbal angles, the control derivative matrix needed to be scaled to avoid the loss of rank in numerical simulations. To achieve this, nonlinear DC-X dynamics were linearized about nominal values corresponding to the steady hover (gimbal angles and RCS equal to zero, total main engine thrust balancing gravity). A change of coordinates for the main engine thrust and RCS further improved the conditioning of the controller so that all inputs maintained the same order of magnitude. The plant position dynamics remained fully nonlinear, whereas the plant attitude dynamics were approximated by a linear model.

A Simulink model of the DC-X dynamics that was used in the hardware-in-the-loop testing is shown in Fig. 6. This model was a slightly simplified version of a full high-fidelity model of the DC-X dynamics furnished by Boeing.

The baseline test scenario was chosen to be a climb–translate–descend maneuver typical for VTOLs. The reference inputs in all three axes are shown in Fig. 7a.

The baseline controller for this model, described in the previous sections, was designed to achieve effective control in all 6 deg of freedom and provide accurate tracking of the desired trajectories. A typical response using the baseline controller is shown on Fig. 7b. Very similar results were obtained with the FLARE-based reconfigurable controller in the case of known failures. The more realistic case of testing under unknown failures is described in the following sections.

## VII. Hardware-in-the-Loop Test Bed Setup

As a part of this project, Boeing provided a test bed and testing time and support in their Facility for Integration and Research of Subsystems Technologies (FIRST Laboratory), Fig. 8. With the help of NASA, a decommissioned unmanned combat air vehicle system A EMA, was obtained and used in conjunction with the EMA test bed, Fig. 9, as a part of the overall HWIL setup.

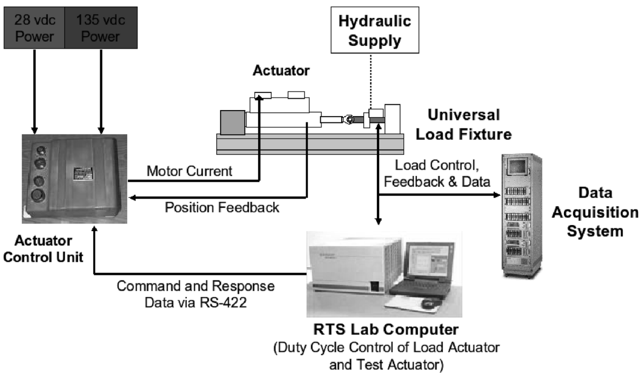

**Fig. 8 Data flow diagram in FIRST Laboratory for testing real-time systems (RTS) (courtesy of Boeing Phantom Works).**

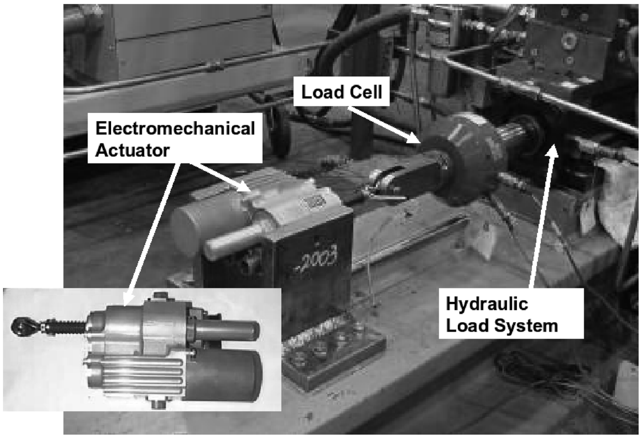

**Fig. 9 EMA in test fixture at Boeing FIRST Laboratory (courtesy of Boeing Phantom Works).**

### A. Fault Injection and Emulation

The high-fidelity DC-X simulation was used to emulate the DC-X dynamics, in which one of the simulated gimbal actuators was replaced by the actual EMA in a setup shown in Fig. 10. The setup had the following provisions for fault injection and emulation:

1) The output of the EMA was attached to a hydraulic load system. Load is required to represent the force due to the weight of the thruster to be actuated. To emulate a LIP failure, the hydraulic system is simply commanded to hold its position.

2) The three-phase motor had one of the phases rewired with switches inserted on each set of windings such that each of the four windings could be shorted individually to emulate an LOE failure (e.g., the coil could be failed partially to 25, 50, and 75%). Because two of the coils remained fully functional, the net effect of failing one coil reduces effectiveness to at most 67%.

3) To increase the range of the loss of effectiveness, a signal is added to the actuator command channel that could overwrite the input commands to the hardware. This allowed failure scenarios such as driving the actuator's response to hardover at the low (HL) or high (HH) position or multiplying the input command by a gain to emulate failures with LOE for which the effect is larger than that corresponding to a single coil failing.

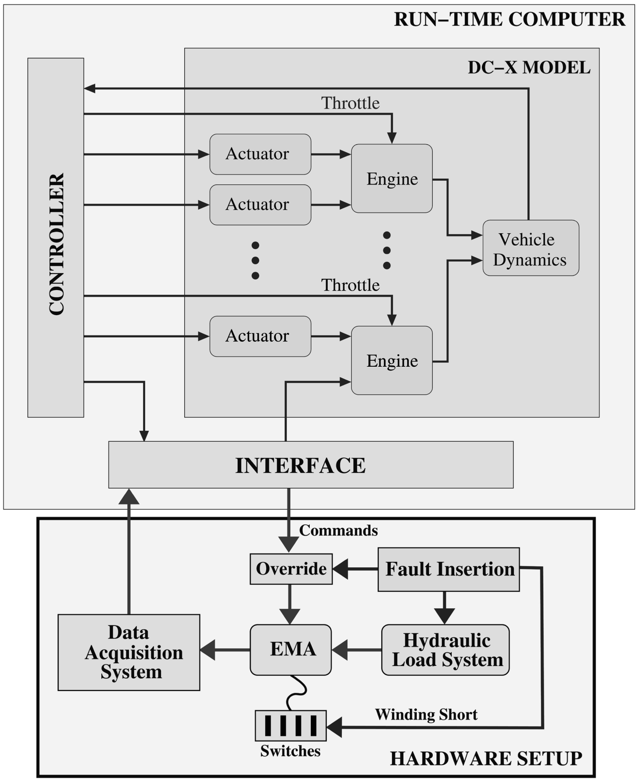

**Fig. 10 HWIL experimental test bed including provisions for overwriting or altering actuator commands, failing windings on a motor coil, and applying a load to the EMA.**

### B. Testing Procedure

Because the controller was designed to accommodate both LOE and LIP failures, a test regime of increasingly drastic failures was designed to evaluate the spectrum of faults that the controller could tolerate. The failures were injected at 20 s (during the ascent portion of the trajectory), which was observed to be the worst time of failure for this particular trajectory.

Before online failure estimation was included in the simulation, the controller was first validated using known failures. Once the robustness of the scheme was established under different failures, the

**Table 2 DC-X simulation LIP, hardover, and LOE failure matrix results. Entries appended with "d" denote the simulation was terminated prematurely due to the attitude violation. For the LOE failures, the values of the LOE coefficients used in the simulations are included in the table**

| Simulation performance results | | | | | | | | | | | | |
|---|---|---|---|---|---|---|---|---|---|---|---|---|
| Failure mode | | | Performance with baseline controller | | | | | Performance with reconfigurable controller | | | | |
| | Actuator no. | Failure type | Max angles, deg | | | Tracking error, m | | Max angles, deg | | | Tracking error, m | |
| | | | Pitch | Yaw | Roll | Max | Final | Pitch | Yaw | Roll | Max | Final |
| | | *LIP/Hardover* | | | | | | | | | | |
| I | 1,5,9 | LIP,LIP,LIP | 2.1 | 9.4 | 8.9 | 22.9 | 9.4 | 0.5 | 4.2 | 0.8 | 4.1 | 1.4 |
| II | 1, 2, 3 , 5, 6, 7, 8, 11, 12, 15 | all LIP | 24.7 | 25.8 | 113.7 | 223.2 | 223.2 | 12.1 | 2.1 | 24.1 | 8.2 | 2.0 |
| III | 1,5,9 | LIP, HL, LIP | 2.1 | 56.2d | 8.9 | 26.4 | 16.5 | 0.5 | 43.3d | 1.3 | 5.1 | 2.0 |
| IV | 1,5,9 | HL, LIP, LIP | 2.3 | 33.7 | 9.9 | 75.5 | 41.5 | 0.5 | 35.2 | 1.1 | 13.6 | 3.4 |
| V | 1,5,9 | LIP, HL, HL | 57.1d | 56.3d | 249.6 | 30.5 | 25.1 | 56.9d | 43.1 | 214.2 | 6.8 | 3.8 |
| VI | 1,5,9 | LIP, HH, LIP | 2.1 | 51.0d | 8.8 | 22.1 | 15.4 | 0.5 | 50.1d | 1.1 | 5.5 | 2.2 |
| VII | 1, 5, 9 | LIP, HH, HH | 44.8 | 49.8d | 204.53 | 2.24 | 1.88 | 49.4d | 41.7 | 228.53 | 7.49 | 7.49 |
| VIII | 5 | HH | 0.4 | 39.4 | 0.0 | 13.1 | 11.64 | 0.4 | 49.4 | 0.0 | 6.0 | 1.8 |
| | | *Loss of effectiveness* | | | | | | | | | | |
| IX | 1,5,9 | 0.5, 0.5, 0.5 | 1.6 | 3.9 | 6.0 | 7.0 | 5.6 | 0.9 | 6.4 | 4.2 | 4.1 | 1.5 |
| X | 1,5,9 | 0.25, 0.5, 0.75 | 0.7 | 6.3 | 2.9 | 10.6 | 9.7 | 0.5 | 2.5 | 2.1 | 4.2 | 1.7 |
| XI | 1,5,9 | 0.75, 0.75, 0.75 | 0.8 | 1.8 | 2.9 | 4.9 | 2.6 | 0.5 | 0.8 | 2.1 | 3.8 | 1.1 |
| XII | 1,5,9 | 0.25, 0.25, 0.25 | 2.6 | 6.4 | 9.5 | 10.6 | 9.7 | 1.2 | 2.5 | 6.3 | 4.2 | 1.7 |
| | | *Gradual degradation* | | | | | | | | | | |
| XIII | 1,5,9 ($\lambda = 0.2$) | 0.5, 0.5, 0.5 | 1.6 | 3.9 | 6.0 | 7.0 | 5.6 | 0.9 | 6.4 | 4.2 | 4.1 | 1.5 |
| XIV | 1,5,9 ($\lambda = 1.0$) | 0.5, 0.5, 0.5 | 1.4 | 3.9 | 5.0 | 7.0 | 5.6 | 0.6 | 6.1 | 2.6 | 4.1 | 1.5 |
| XV | 1,5,9 ($\lambda = 10.0$) | 0.5, 0.5, 0.5 | 0.9 | 3.9 | 3.2 | 7.0 | 5.5 | 0.6 | 7.4 | 3.6 | 4.1 | 1.5 |

failure estimators were included in the closed loop and tuned for acceptable performance.

After a series of exploratory simulations were performed in-house on the high-fidelity simulation of DC-X, the resulting "well-tuned" controller was used in the HWIL tests. A variety of test cases representing a spectrum of EMA and simulated EMA malfunctions were incorporated into a test matrix for comparison. These tests determined which combinations of failures significantly affected the system dynamics. For example, due to the redundancy of the control actuators, preliminary tests indicated that single-point actuator degradation led to very little performance loss. These results indicate that the nominal system is robust to single failures even with no control reconfiguration taking place. To make the effects of the failures more pronounced, failures were introduced in clusters to test the robustness of the controller.

The failure matrix for both simulation and HWIL testing included failures to the EMA coupled with failures in actuator simulation models. This coupling resulted in a more pronounced effect of the multiple failures on the response of the system. The failure matrix included LIP, hardover (high and low), theoretical controllability limit (all but six actuators locked), and various degrees of LOE. A subset of the LOE failures included loss of effectiveness due to winding shorts alone and winding shorts coupled with the downscaled inputs (i.e., inputs multiplied by gains less than 1). To explore the effect of the gradual degradation of actuator performance, a set of experiments was also run in which the actuator effectiveness was decreased either continuously or at discrete steps.

## VIII. Simulation Results

Sample simulation results are presented in Table 2, and hardware in the loop simulation results are found in Table 3. The actuators are numbered 1–16, with four main engines labeled 1–4, four radial gimbal angles labeled 5–8, four tangential angles labeled 9–12, and four RCS thrusters labeled 13–16, as designated in the schematics in Figs. 3 and 4.

The tables are organized as follows:

1) Left columns describe the failure modes introduced in the actuators. The left subcolumn lists the identification numbers of the actuators that were failed during a specific simulation run. The right subcolumn lists corresponding failures. For instance, cases I–VIII correspond to the LIP and hardover failures. As an example, in row IV, actuators 1, 5, and 9 in the left subcolumn are combined with HL and LIP, LIP indicating that in that run actuator 1 underwent a lower hardover, whereas actuators 5 and 9 underwent LIP failures.

2) The central column shows attitude errors during a run, along with the maximum tracking error in the case of the baseline controller with failure cases described in the left column.

3) The right column shows the errors in the case of the reconfigurable controller for the same failure case. Effectiveness of the reconfigurable controller can be evaluated by directly comparing error columns within the same row.

4) Rows IX–XII show the results in the case of LOE failures. The left column lists failure modes with the left subcolumn listing the identification numbers of the actuators that were failed during a run. The right subcolumn lists the LOE coefficients of those actuators. For instance, row X lists actuators 1, 5, and 9 and the corresponding LOE coefficients of 0.25, 0.5, and 0.75, that is, actuator 1 had a LOE of 0.25, actuator 5 of 0.5, and actuator 9 of 0.75.

5) Rows XIII–XV show results under slow degradation in actuators 1, 5, and 9. Slow degradation is described as the following change in the actuator gain:

$$k(t) = \begin{cases} 1, & \text{if } t < t_f, \\ 0.5 + 0.5e^{-\lambda(t-t_f)} & \text{if } t \geq t_f \end{cases} \tag{27}$$

It is seen that all actuators start with gains equal to 1, whereas the degradation starts at time $t_f$, and its response is dictated by the constant $\lambda$. The LOE coefficient stays between 0.5 and 1. Rows XIII–XV show the results for three different values of $\lambda$.

For the sake of comparison, the results obtained using the baseline controller are given alongside those obtained using the reconfigurable controller. The table includes the maximum rotation about each axis, the maximum tracking error, and the final tracking error. Pitch and yaw angles greater than 45 deg are considered unacceptable. Included in the table is an array of failure tests that represent the basic LIP/hardover on inputs to one of the gimballed engines, basic LOE, and basic performance degradation both continuously (denoted "c") and in steps (denoted either "5" or "3" to refer to five or three steps).

**Table 3 DC-X HWIL LIP, hardover and LOE failure matrix results. For the LOE failures, the values of the LOE coefficients used in the HWIL simulations are included in the table. Gradual degradation on actuator 5 was accomplished either continuously ("c") or in 3 or 5 steps**

| HWIL simulation performance results | | | | | | | | | | | | |
|---|---|---|---|---|---|---|---|---|---|---|---|---|
| Failure mode | | | Performance with baseline controller | | | | | Performance with reconfigurable controller | | | | |
| | Actuator no. | Failure type | Max angles, deg | | | Tracking error, m | | Max angles, deg | | | Tracking error, m | |
| | | | Pitch | Yaw | Roll | Max | Final | Pitch | Yaw | Roll | Max | Final |
| | | *LIP/hardover* | | | | | | | | | | |
| I | 1,5,9 | LIP, LIP, LIP | 2.09 | 9.57 | 8.89 | 23.09 | 9.46 | 0.45 | 4.21 | 0.75 | 2.26 | 0.6 |
| II | 1,2,3,5,6,7,8,11,12,15 | all LIP | 24.59 | 25.69 | 113.28 | 222.64 | 222.64 | 12.14 | 7.35 | 24.16 | 7.27 | 1.15 |
| III | 1,5,9 | LIP, HL, LIP | 2.1 | 49.18 | 8.93 | 314.97 | 14.86 | 0.45 | 41.12 | 1.02 | 3.68 | 1.34 |
| IV | 1,5,9 | HL, LIP, LIP | 2.31 | 33.71 | 9.86 | 75.55 | 41.58 | 0.5 | 33.99 | 1.15 | 14.67 | 3.9 |
| V | 1,5,9 | LIP, HL, HL | 62.21 | 49.35 | 271.21 | 29.46 | 23.44 | 47.32 | 11.47 | 213.14 | 4.63 | 3.23 |
| VI | 1,5,9 | LIP, HH, LIP | 2.07 | 44.23 | 8.8 | 21.74 | 14.53 | 0.45 | 47.13 | 1.05 | 4.34 | 1.52 |
| VII | 1,5,9 | LIP, HH, HH | 55.14 | 44.07 | 240.72 | 25.92 | 24.52 | 29.38 | 41.31 | 199.84 | 6.47 | 3.74 |
| VIII | 5 | HH | 0.43 | 34.68 | 0.0 | 11.94 | 10.65 | 0.43 | 41.89 | 0.0 | 3.67 | 1.47 |
| | | *Loss of effectiveness* | | | | | | | | | | |
| IX | 1,5,9 | 0.5,0.5,0.5 | 1.39 | 3.84 | 5.03 | 5.94 | 5.47 | 0.6 | 6.42 | 2.6 | 1.53 | 0.7 |
| X | 1,5,9 | 0.25,0.5,0.75 | 0.64 | 6.2 | 2.37 | 10.31 | 9.58 | 0.43 | 2.51 | 2.9 | 1.77 | 0.99 |
| XI | 1,5,9 | 0.75,0.75,0.75 | 0.64 | 1.69 | 2.37 | 2.72 | 2.45 | 0.43 | 0.85 | 2.91 | 1.25 | 0.37 |
| XII | 1,5,9 | 0.25,0.25,0.25 | 2.26 | 6.31 | 8.11 | 10.33 | 9.61 | 0.94 | 2.52 | 3.89 | 1.75 | 0.99 |
| | | *LOE healthy windings* | | | | | | | | | | |
| IXa | 1,5,9 | 0.5,0.5,0.5 | 1.39 | 3.79 | 5.03 | 5.94 | 5.47 | 0.6 | 6.33 | 2.6 | 1.51 | 0.7 |
| Xa | 1,5,9 | 0.25,0.5,0.75 | 0.64 | 6.18 | 2.37 | 10.31 | 9.58 | 0.43 | 2.49 | 2.97 | 1.77 | 0.99 |
| XIa | 1,5,9 | 0.75,0.75,0.75 | 0.64 | 1.68 | 2.37 | 2.72 | 2.45 | 0.43 | 0.83 | 2.92 | 1.25 | 0.37 |
| XIIa | 1,5,9 | 0.25,0.25,0.25 | 2.26 | 6.52 | 8.11 | 10.35 | 9.64 | 0.93 | 2.49 | 3.89 | 1.75 | 0.99 |
| | | *Gradual degradation* | | | | | | | | | | |
| XIII | 1,5,9 | 0.25, c, 0.25 | 2.26 | 6.53 | 8.11 | 10.32 | 9.64 | 0.94 | 2.53 | 3.94 | 1.72 | 0.99 |
| XIV | 1,5,9 | 0.25, 5, 0.25 | 2.26 | 6.53 | 8.11 | 10.3 | 9.64 | 0.96 | 2.53 | 3.92 | 1.73 | 0.99 |
| XV | 1,5,9 | 0.25, 3, 0.25 | 2.26 | 6.52 | 8.11 | 10.28 | 9.64 | 0.95 | 3.06 | 3.94 | 1.73 | 0.99 |

Figures 11a–11c, which depict failure case I in the table, show the states, estimates, and inputs, respectively, for the reconfigurable controller with LIP failures at actuators 1, 5, and 9. The plots from the other simulation cases from Table 2 look very similar to the included results.

## IX. Hardware-in-the-Loop Testing Results

All cases from Table 2 have corresponding HWIL test cases listed in Table 3. The only exception is the case of gradual degradation, in which, in the case of HWIL, instead of using the dynamics (27), we used the following:

Row XIII

$$k(t) = \begin{cases} 1, & \text{if } t < 20, \\ 1 - 0.03(t-20) & \text{if } t \geq 20 \text{ and } t < 50 \\ 0.1, & \text{if } t \geq 50 \end{cases} \tag{28}$$

Row XIV

$$k_5(t) = \begin{cases} 1 & \text{if } t < 20 \\ 1 - 0.18i & \text{if } t \geq t_f + 6i, \qquad i = 1, 2, \ldots, 5 \end{cases} \tag{29}$$

Row XV

$$k_3(t) = \begin{cases} 1 & \text{if } t < 20 \\ 1 - 0.3i & \text{if } t \geq t_f + 10i, \qquad i = 1, 2, 3 \end{cases} \tag{30}$$

The reason is that these changes are to test a more severe case and were a good test case for performance evaluations. Tests IXa–XIIa were duplicate tests of IX–XII, but without any of the physical windings in the EMA being shorted. Rather, software-only failures were introduced. The state response for each of the tests looked similar to the plots in Fig. 12, which represents LIP failure at actuators 1, 5, and 9.

In Fig. 13, parameter estimates for cases IX and I, respectively, are shown, for which the top three plots of each subfigure are the estimated failure parameters for actuators 1, 5, and 9, respectively, whereas the fourth one shows which multiple-model estimator is active for each actuator.

When all actuators are at least partially functional, as in case IX, the inputs look similar to those in Fig. 14a. The inputs in Fig. 14b are from a simulation performed from failure case II, which corresponds to the theoretical limit of controllability, that is, 6 deg of freedom

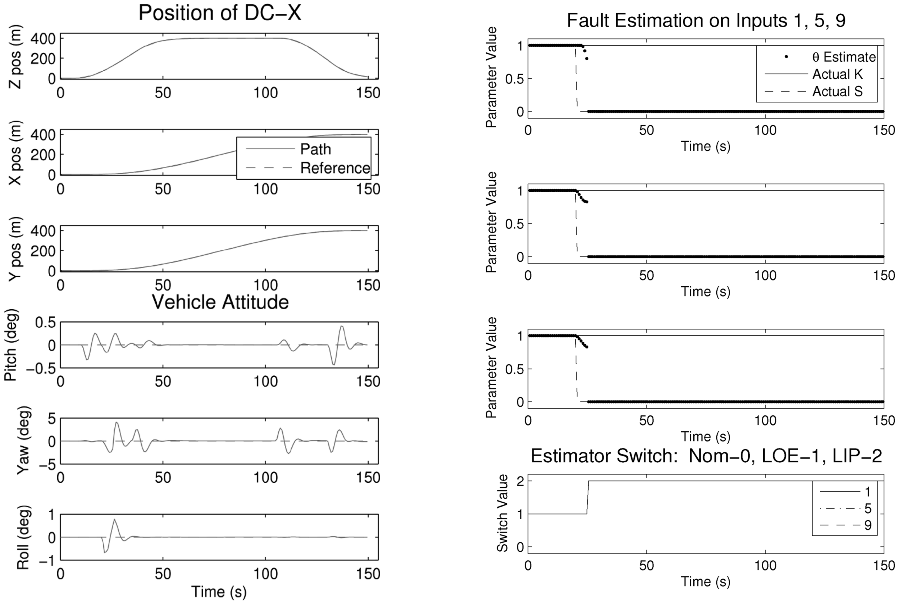

**a) Typical trajectory with LIP on actuators 1, 5, 9** **b) Estimation, LIP 1, 5, 9**

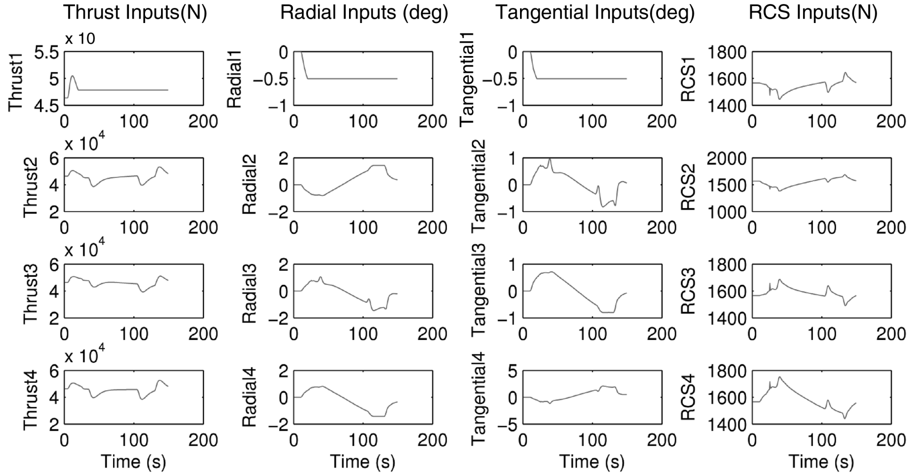

**c) Inputs for LIP failure case at 1, 5, 9**

**Fig. 11 Typical simulation inputs and estimates given mild and severe failures (case I). In Figs. 11a–11c, actuators 1, 5, and 9 are locked in place at the time of failure and the states were held under tight control while the observers correctly identified the failures. The inputs reflect active control under this scenario.**

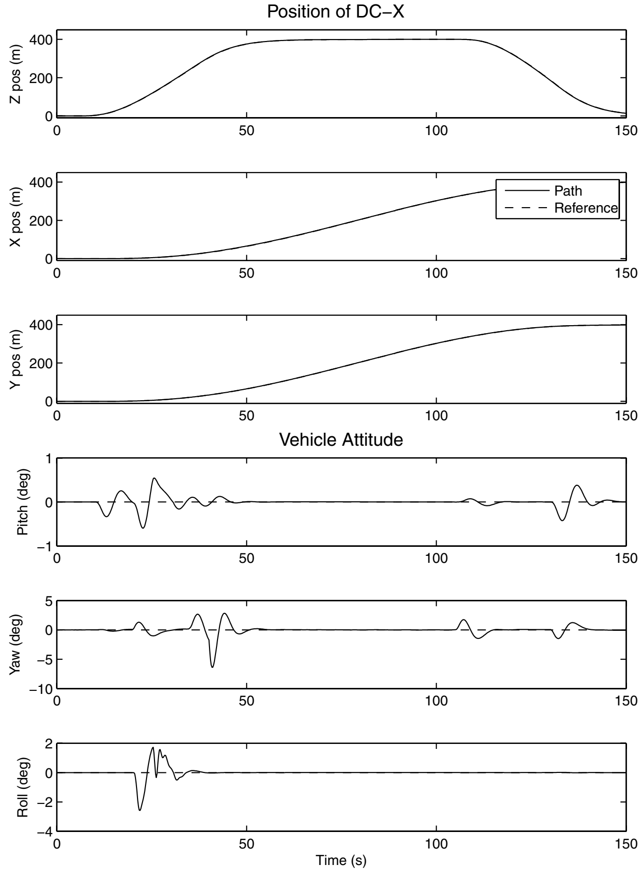

**Fig. 12 DC-X state response from a typical simulation. The climb, translate, and descend maneuvers were accomplished with very little angular perturbations in this example of the baseline controller performing under no failures.**

were controlled using only six actuators (10 actuators are failed). The plots from the other simulations in Table 2 look very similar to the included results.

Figure 15 shows results as the magnitude of the injected failure to the HWIL actuator decreased with time. The plots show how the failure parameter estimates converge with continuous failure, case XIII; failure in five steps, case XIV; and failure in three increments, case XV.

The most severe failures introduced to the system were hardover failures. Sample results from various hardover failure cases, including cases I, III, IV, and VII, are shown in Fig. 16.

## X. Discussion of Results

As anticipated, in the case of failures, the reconfigurable controller outperformed the baseline controller in tracking position and attitude. For the simulations that were not terminated early due to failure, the states in large part resemble those in Fig. 12. Only minor variations in the magnitude of the transient response caused by the changes in acceleration were evident in other plots of states.

### A. Special Failure Cases and General Observations

The following subsections describe the performance of the multiple-model controller and characteristics of observed responses to the experiments that can be attributed to particular failure types.

#### *1. Lack of Identifiability*

Analysis of the plant affirms that the gimballing actuators are linked to specific body-frame translations and rotations. For example, it is apparent that failures of actuator 10 (the 12 o'clock tangential EMA, $\alpha_{T2}$) are tied to translations in $x$ and yaw rotations. Hence, the persistent excitation to adapt the failure parameter on actuator 10 is not available until the trajectory requires the actuator contribute to $x$ translation. Furthermore, holding a command does not provide sufficient persistent excitation for estimate convergence. Trajectories that require continuous motion of inputs to the actuators yield more accurate estimates. This concept lends itself to another observation that the vehicle's response to failure depends largely on the trajectory required for the vehicle: failure of an unused actuator results in no appreciable change in vehicle behavior.

#### *2. Accommodation of Multiple Failures*

Both simulation and HWIL results revealed that the reconfigurable controller is able to accommodate many cases of multiple severe failures. However, in some cases the attempted control reconfiguration may exhaust the available control authority. For instance, when the maneuver requires the control authority that is already close to its limit and multiple failures occur, the reconfigurable controller may fail to achieve the control objective. In addition, accommodation of hardover failures requires very large control authority. Such control authority is not available in DC-X in the case of two or more hardover failures.

#### *3. LIP Failures*

The results organized in Tables 2 and 3 indicate that in every case the reconfigurable controller outperformed the baseline controller in terms of tracking the trajectory while maintaining nominal attitude. The assortment of LIP failures resulted in maximum tracking error between 3.9 and 8.2 m for the reconfigurable controller compared with a 6.2–278.4 m maximum error for the baseline controller. In no cases did the reconfigurable controller violate the acceptable attitude criteria, whereas two of the 11 tests with the baseline controller failed.

As shown in Fig. 14b, the plant has sufficient redundancy not to saturate the control inputs. With all but six actuators locked into place midmaneuver, the remaining six actuators maintain 6 deg of freedom trajectory tracking for the rest of the maneuver. We recall that the system has 16 actuators, 10 of which are redundant. However, as noted earlier, this redundancy is contingent upon the demands of the trajectory and the status of the actuators at the time of failure.

#### *4. Hardover Failures*

Failures of an even more drastic type, such as hardover actuator failures (see Sec. III) have potentially devastating results. Both controllers were able to mitigate a hardover full throttle engine, though the reconfigurable controller tracked the desired trajectory much better (baseline: 75.5 m error, reconfigurable controller: 13.6 m error). Hardover failures on the EMA-driven angles result in unacceptable performance in the case of the baseline controller. Even though the reconfigurable controller is able to neutralize one EMA hardover failure while meeting attitude constraints, an additional hardover failure on a different actuator at a different part of the trajectory might prove catastrophic. Two hardover failures cause both controllers to fail.

#### *5. Partial Actuator Failures*

Amid partially failed actuators, tabulated in the lower half of Table 3, our FDIR system is capable of accurately identifying and accommodating the failures. As with the results from LIP failures, the reconfigurable controller outperforms the baseline in all cases. Failures closer to zero (e.g., 0.25 or less) were observed to produce results that resemble LIP failures.

#### *6. Response with the Baseline Controller*

The baseline controller is also observed to perform very well amidst the host of failures. This fact arises from the available control authority generated by the redundant actuators. However, severe failures were generally accommodated more effectively using the reconfigurable controller, whereas the baseline controller would either result in instability or in substantial performance deterioration.

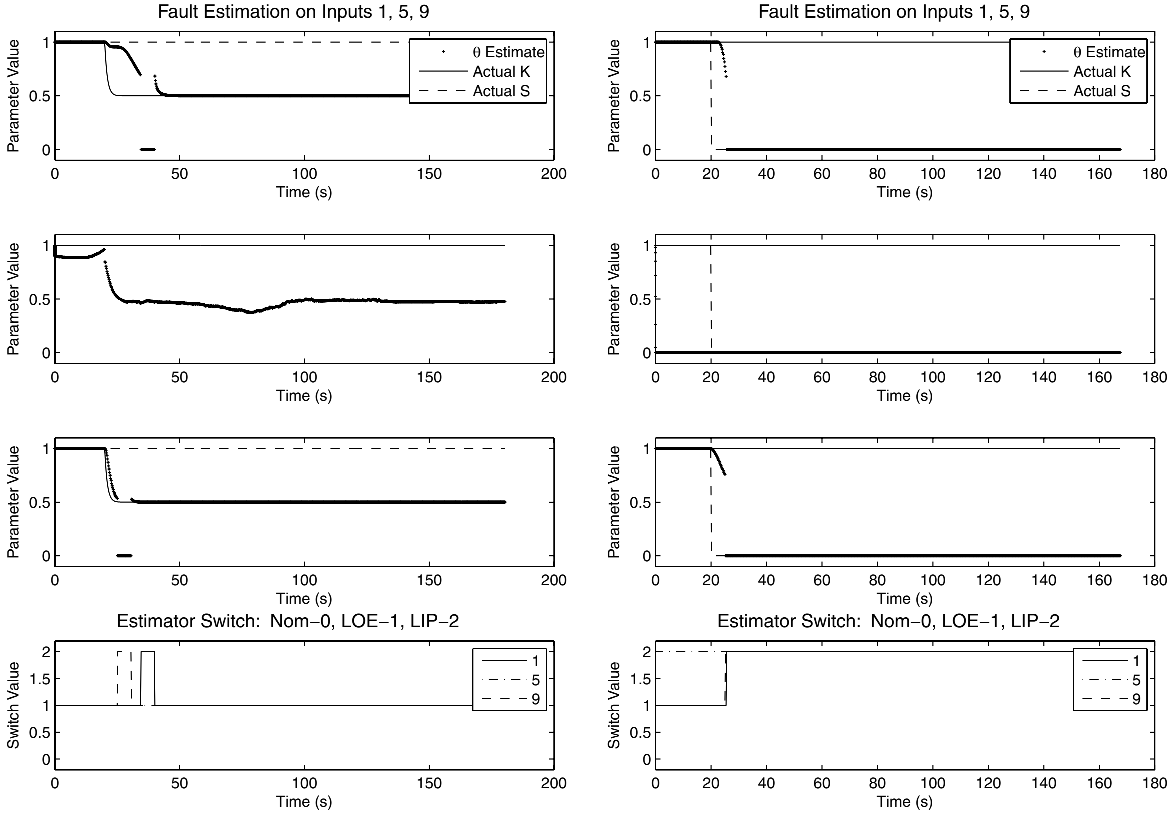

a) LOE 0.5, 0.5, 0.5, case IX b) LIP 1, 5, 9, case I

**Fig. 13 HWIL estimates of failure parameters for actuators 1, 5, and 9. In both the loss-of-effectiveness and lock-in-place cases, the estimators quickly identify the correct failure parameters. The top three plots of each subfigure are the failure parameter estimates for actuators 1, 5, and 9, respectively, whereas the fourth one shows which multiple-model estimator is active for each actuator. In both cases the correct estimator arrives at an accurate estimate within just a few seconds after the failure.**

### 7. *Estimator Performance*

The multiple-model failure estimators were observed to result in fast convergence of failure-related parameters. For the LOE tests presented in the paper, a time constant was chosen such that the performance of the actuator was reduced over a period of 5 s. Therefore, within 5 s of failures being introduced, insofar as the system experienced sufficient excitation, the estimate also converged. Amid lack of excitation, the estimate was shown to wander about 10% from the actual. Initial uncertainties caused the initial "health" value to begin around 80% until the simulation was fully underway.

## B. Comparison of Simulation and Experimental Results

Comparisons of the simulation results in Table 2 with those obtained through experiments in Table 3 reveal that the HWIL results very closely match results obtained through high-fidelity simulations performed in-house at Scientific Systems Company, Inc. Based on these results, the following observations can be made:

1) The HWIL results for *lock-in-place failures* were consistent with the simulation results, and similar performance improvement was observed in both cases with respect to the response obtained using the baseline controller.

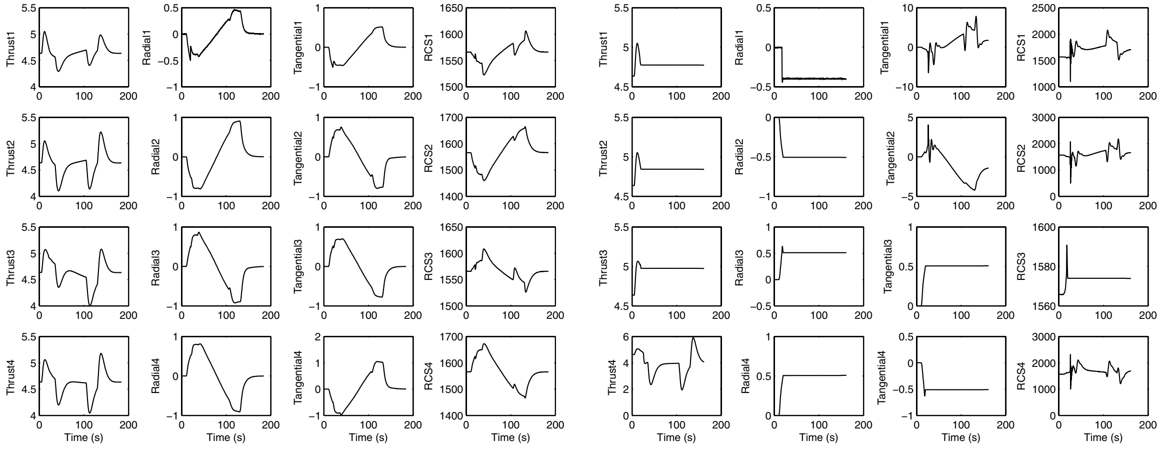

a) LOE 0.5, 0.5, 0.5, case IX b) Limit of stability, case II

**Fig. 14 HWIL DC-X inputs commands when reconfiguring for LOE failures and reconfiguring for LIP to 10 actuators. In Fig. 14a, the failed actuators can still have effect by increasing their command. However, when the actuators are locked up, as in Fig. 14b, the remaining actuators must make up the difference for the 10 locked actuators.**

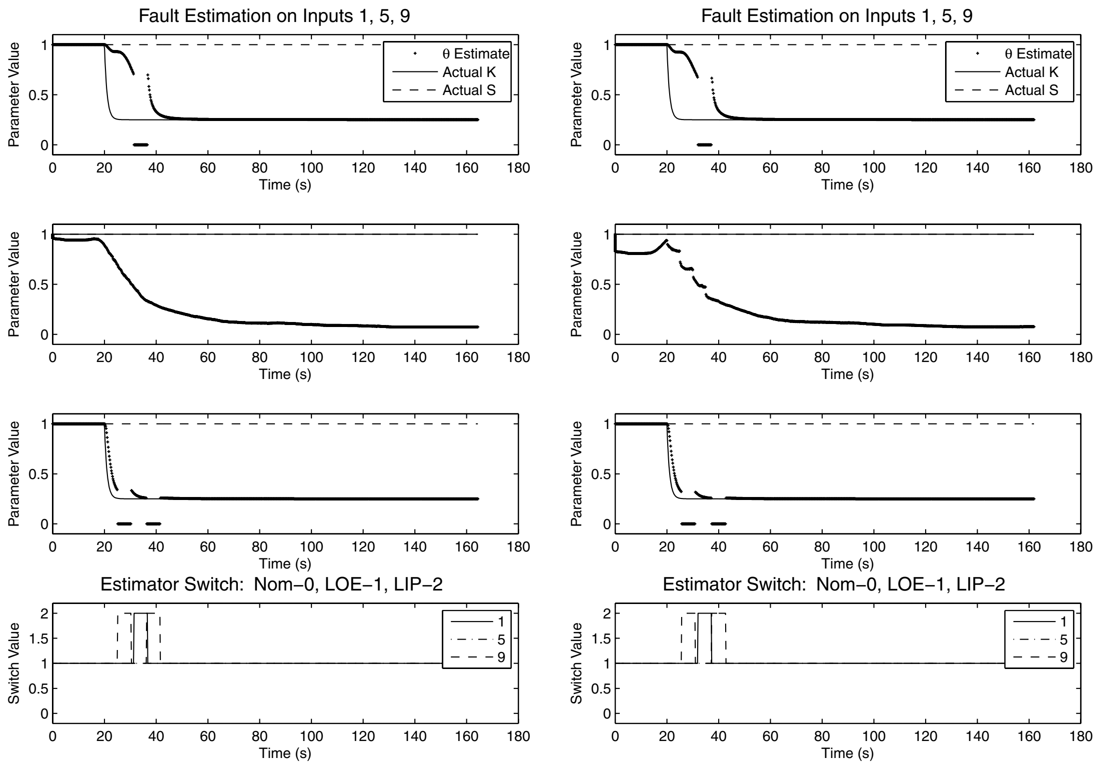

**a) HWIL case XIII** **b) HWIL case XIV**

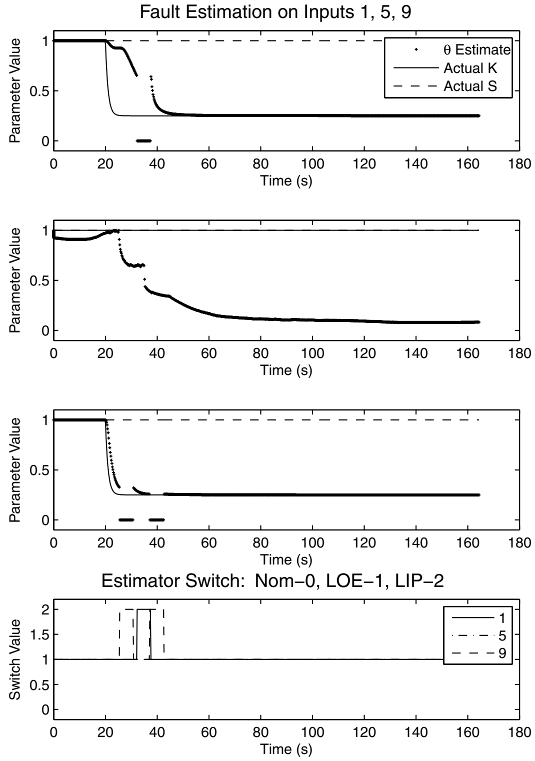

**c) HWIL case XV**

**Fig. 15 LOE estimates with gradual decay on HWIL actuator. Early failures prevent initialization at full health. The top three plots are the outputs of the estimators on actuators 1, 5, and 9, respectively, whereas the fourth shows which estimator is active for each actuator.**

2) In both cases, *hardover failures*, whether at the high or low endpoint, were often too severe to accommodate with available control authority. Although in some cases single actuator hardover could be compensated for, multiple hardover failures would generally cause saturation of the remaining healthy actuators, resulting in closed-loop system instability.

3) The basic HWIL results in the cases of actuator *loss of effectiveness* correspond to tests run with half of the windings shorted on one of the EMA motor coils, in addition to the lower gain values applied to the actuator input. The results are consistent with the observations from the simulations. Although LOE failures in the motors were effectively emulated via shorting the windings within

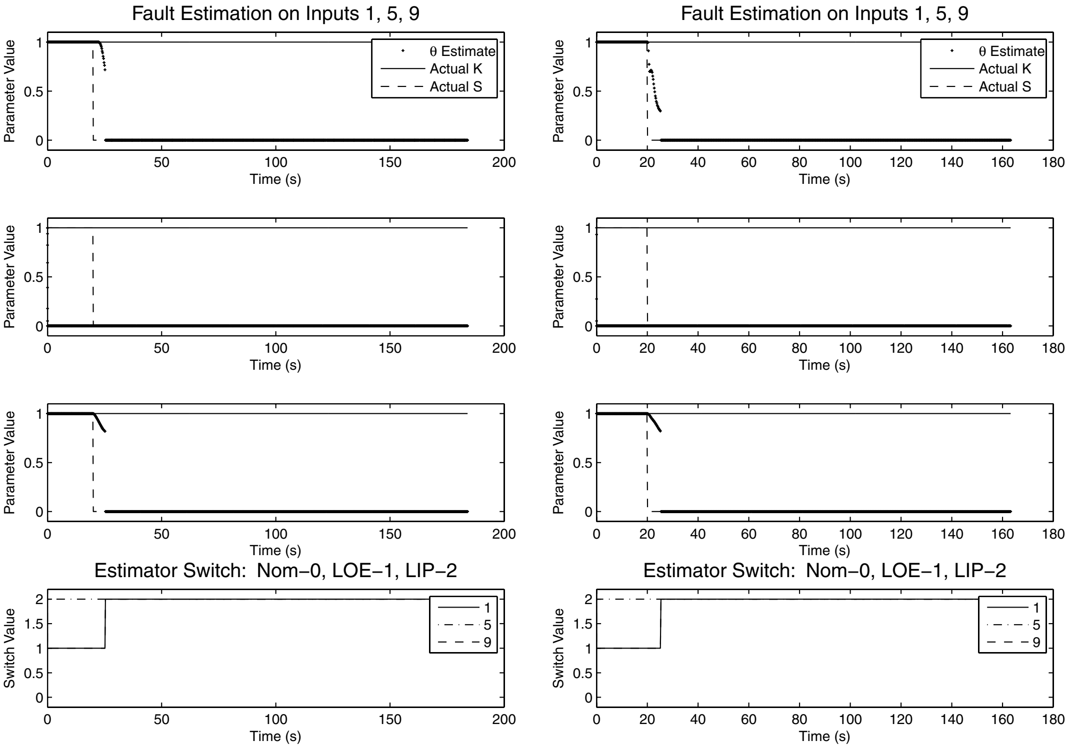

**a) LIP on 1, 5, and 9, HWIL case I** **b) LIP on 1 and 9, hard-over high on 5, HWIL case VI**

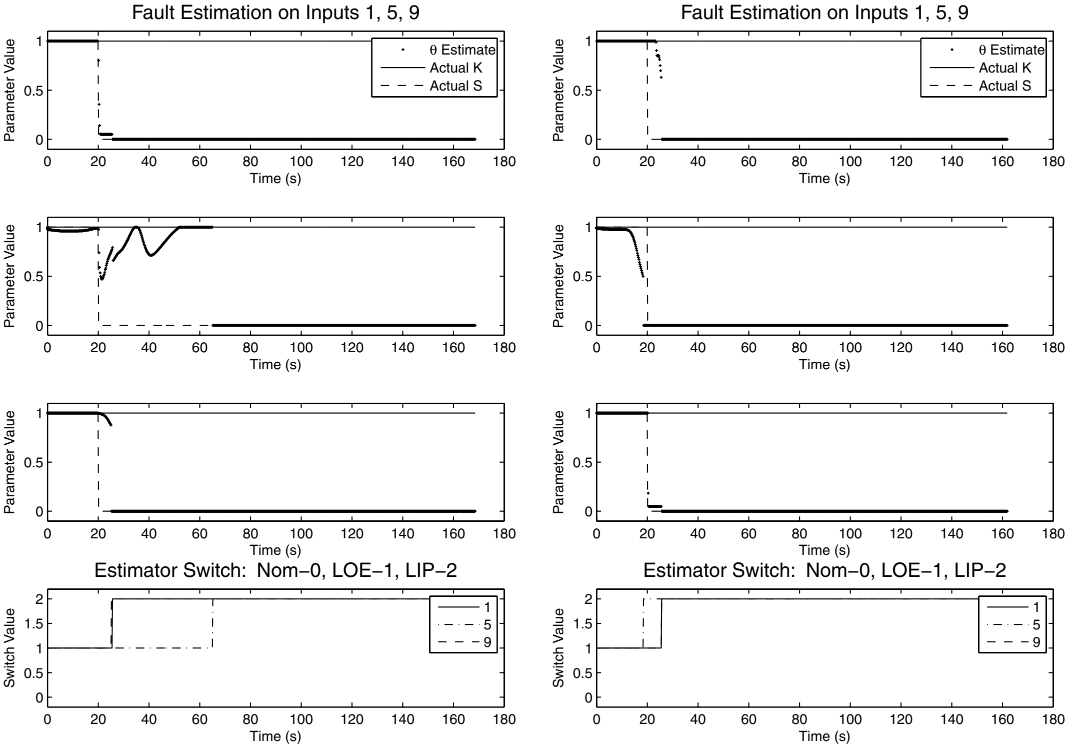

**c) Hard-over low on 1, LIP on 5 and 9, HWIL case IV** **d) LIP 1, hard-over high on 5 and 9, HWIL case VII**

**Fig. 16 LIP/HO estimates on the HWIL actuator. The top three plots are the outputs of the estimators on actuators 1, 5, and 9, respectively, whereas the fourth shows which estimator is active for each actuator.**

the coil, this barely resulted in any loss of performance as no appreciable differences were observed between the HWIL experiments using healthy and shorted windings.

4) During the HWIL tests in the case of *gradual degradation of actuator performance*, that is, gradual decrease in the actuator gain, the scenario also included failures of two software actuators. In all cases the corresponding estimator was able to accurately identify gradual changes in the actuator gain, and the use of these estimates in the control law resulted in excellent overall performance. This property of the estimators is also important for health monitoring and *prognostics*. In the latter case, based on estimates of the actuator gain over a time interval, it is possible, at least approximately, to predict the time when the actuator will completely lose effectiveness. This may indicate the useful life remaining before the actuator needs to

be replaced and may play an important role in condition-based maintenance.

In conclusion, the HWIL tests were successful in demonstrating effective fault detection, identification, and subsequent controller reconfiguration using the FLARE system within a setup that included an EMA actuator as a part of the simulation of DC-X dynamics. The multiple-model estimator provided estimates of failure parameters that were very close to the actual values, and the overall HWIL system behavior was seen to be consistent with that observed during the high-fidelity simulations.

## XI. Conclusions

In this paper, an FDIR control scheme is developed for a dynamic model of the DC-X7 single stage to orbit/planetary lander rocket concept. The 6 deg of freedom redundantly actuated model provides a well-suited test case for designing a controller for actuators with different response rates using a multiple-model failure parameter estimation method. Even under multiple severe flight-critical failures, the reconfigurable controller was shown through high-fidelity simulations to maintain the desired closed-loop performance. Robustness of the system was demonstrated under a large number of different single and multiple failure cases.

The simulations presented here used a linearized controller. Future studies incorporating the dynamic nonlinear controller and a high-fidelity nonlinear plant model are anticipated to provide insight into the capabilities of the proposed system to handle failures in the nonlinear flight regimes and over an enlarged flight envelope. Although greater controller and model complexity may provide better tracking over larger failure sets, we note that in the all cases except hardover failures the linearized reconfigurable controller performed extremely well. Hence, a study related to the use of different controllers in different regions of the state or parameter space may be of interest. A suitable framework for the corresponding reconfigurable control design might be based, for instance, on the concept of multiple models, switching, and tuning [15].

## Acknowledgments

We would like to extend our sincere thanks to Kirby Keller, Jeremy Gaither, and Jim Sheahan at Boeing Phantom Works for providing technical support, the DC-X simulation, and hardware-in-the-loop test facilities for validating the research. This work was supported by NASA under contract NNAAA04C to SSCI.

## References

[1] Bošković, J. D., Prasanth, R., and Mehra, R. K., "Retrofit Reconfigurable Flight Control Under Control Effector Damage," *Journal of Guidance, Control, and Dynamics*, Vol. 30, No. 3, May–June 2007, pp. 703–712.
doi:10.2514/1.25564

[2] Bodson, M., and Groszkiewicz, J., "Multivariable Adaptive Algorithms for Reconfigurable Flight Control," *IEEE Transactions on Control Systems Technology*, Vol. 5, No. 2, March 1997, pp. 217–229.
doi:10.1109/87.556026

[3] Brinker, J., and Wise, K., "Reconfigurable Flight Control of a Tailless Advanced Fighter Aircraft," *Proceedings of the 1998 AIAA Guidance, Navigation and Control Conference*, Vol. 1, AIAA, Reston, VA, Aug. 1998, pp. 75–87.

[4] Calise, A., Lee, S., and Sharma, M., "Direct Adaptive Reconfigurable Control of a Tailless Fighter Aircraft," in *Proceedings of the 1998 AIAA Guidance, Navigation and Control Conference*, Vol. 1, AIAA, Reston, VA, Aug. 1998, , pp. 88–97.

[5] Chandler, P., Pachter, M., and Mears, M., "System Identification for Adaptive and Reconfigurable Control," *Journal of Guidance, Control, and Dynamics*, Vol. 18, No. 3, May–June 1995, pp. 516–524.
doi:10.2514/3.21417

[6] Carter, J., Rachel, J., Corbin, B., and Block, R., "Vehicle Management System for Single Stage Rocket," AIAA Paper 1993-963, Feb. 1993.

[7] Voglewede, S., "Single Stage Rocket Technology's Real Time Data System," *Goddard Space Flight Center, Third International Symposium on Space Mission Operations and Ground Data Systems*, Part 1, NASA, Washington, DC, 1994 pp. 155–168.

[8] Platt, M., "Full Lyapunov Exponent Replacement in Reentry Trajectories," Master's Thesis, Air Force Inst. of Tech, Wright–Patterson Air Force Base, OH, Dec. 1995.

[9] Wiesel, W., "Optimal Pole Placement in Time-dependent Linear Systems," *Journal of Guidance, Control, and Dynamics*, Vol. 18, No. 5, Sept.–Oct. 1995, pp. 995–999.
doi:10.2514/3.21496

[10] Nowlan, D. R., Humphrey, D. S., Pak, Y. H., and Cook, L. M., "Delta Clipper-Experimental (DC-X) GN&C System," *Advances in the Astronautical Sciences*, Vol. 88, 1995, pp. 527–546.

[11] Bošković, J. D., Bergstrom, S. E., Mehra, R. K., Urnes, J. Sr., and Hood, M., and Lin, Y., "Fast on-Line Actuator Reconfiguration Enabling (FLARE) System," AIAA Paper 2005-6339, Aug. 2005.

[12] Bošković, J. D., and Mehra, R. K., "Robust Integrated Flight Control Design Under Failures, Damage and State-Dependent Disturbances," *Journal of Guidance, Control, and Dynamics*, Vol. 28, No. 5, Sept.–Oct. 2005, pp. 902–917.
doi:10.2514/1.11272

[13] Bošković, J. D., Jackson, J., Nguyen, N., and Mehra, R. K., "Multiple Model-Based Adaptive Fault-Tolerant Control of Delta Clipper Experimental (DC-X) Planetary Lander," AIAA Paper 2008-7290, Aug. 2008.

[14] Bošković, J. D., Redding, J., and Mehra, R. K., "Robust Fault-Tolerant Flight Control using a New Failure Parameterization," *Proceedings of the 2007 American Control Conference*, IEEE Publications, Piscataway, NJ, July 2007, pp. 5753–5758.
doi:10.1109/ACC.2007.4282340

[15] Bošković, J. D., and Mehra, R. K., "A Multiple Model Adaptive Flight Control Scheme for Accommodation of Actuator Failures," *Journal of Guidance, Control, and Dynamics*, Vol. 25, No. 4, July–August, 2002, pp. 712–724.
doi:10.2514/2.4938

[16] Narendra, K. S., and Balakrishnan, J., "Adaptive Control Using Multiple Models," *IEEE Transactions on Automatic Control*, Vol. 42, No. 2, February 1997, pp. 171–187.
doi:10.1109/9.554398

[17] Bošković, J. D., Chen, L., and Mehra, R. K., "Adaptive Control Design for a Class of Non-Affine Models Arising in Flight Control," *Journal of Guidance, Control, and Dynamics*, Vol. 27, No. 2, March–April 2004, pp. 209–217.
doi:10.2514/1.1106